Confined turbulent convection driven by a combination of line and distributed sources of buoyancy

Johanna Mader,* Maarten van Reeuwijk, and John Craske
Department of Civil and Environmental Engineering, Imperial College London, London SW7 2AZ, England, United Kingdom

(Received 23 January 2020; accepted 27 October 2020; published 26 February 2021)

We study the flow and thermal stratification of a closed domain subjected to different combinations of line and distributed surface heating and cooling. Our observations are drawn from a set of direct numerical simulations in which the ratio of the strength of the distributed sources to the localized sources Γ is varied and shown to play a decisive role in determining the system's statistically steady state. Domains of sufficient horizontal extent that are heated from below and cooled from above in equal amounts by two line sources ($\Gamma = 0$) produce a stable two-layer stratification. The planar plumes generated by each line source are connected by a large-scale circulation over the full depth of the domain and induce secondary circulations within each layer. As the distributed component of the heating, and therefore Γ, increases, the buoyancy difference between the layers decreases, before being destroyed when $\Gamma > 1$. For increasing $\Gamma \in [0, 1]$, we observe an increasing tilt of the interface between the layers and the eventual disappearance of the secondary circulation cells. The mean buoyancy transport between the two layers of the stable stratification is dominated by the plumes for all $\Gamma < 1$ because the buoyancy flux associated with interfacial mixing is negligible. Building on existing approaches that typically assume uniform buoyancy within each layer, we develop a model that admits a lateral buoyancy gradient. The model predictions of the buoyancy difference between the layers, the tilt of the interface, and the large-scale circulation strength exhibit a reasonably good agreement with the direct numerical simulation data.

DOI: 10.1103/PhysRevFluids.6.023503

I. INTRODUCTION

Configurations of one or multiple plumes arising from localized sources of heat are commonly used to model buoyancy-driven flows in geophysical and engineering applications. A specific example concerns the ventilation and heating of buildings [1–4], where plumes can represent the effect of radiators, air conditioners, electrical appliances, occupants, and/or lighting. More generally, localized sources of heat are found in combination with distributed sources of heat, which raises the question of how the flows resulting from the different types of forcing interact.

The flows and buoyancy structures produced by localized sources of heat differ from those produced by distributed sources. Localized sources result in turbulent plumes [5], which are free-shear flows that entrain and mix fluid from their environments. A confined plume typically leads to a stable stratification of the surrounding environment [6]. In such cases, relatively warm, buoyant fluid accumulates at the top of the space in a layer that deepens and gets warmer [7]. If the total heat input is zero, a statistically steady state can be attained, of which the two-layer stratification created by "equal and opposite" plumes [6,8] is a canonical example.

*j.mader16@imperial.ac.uk

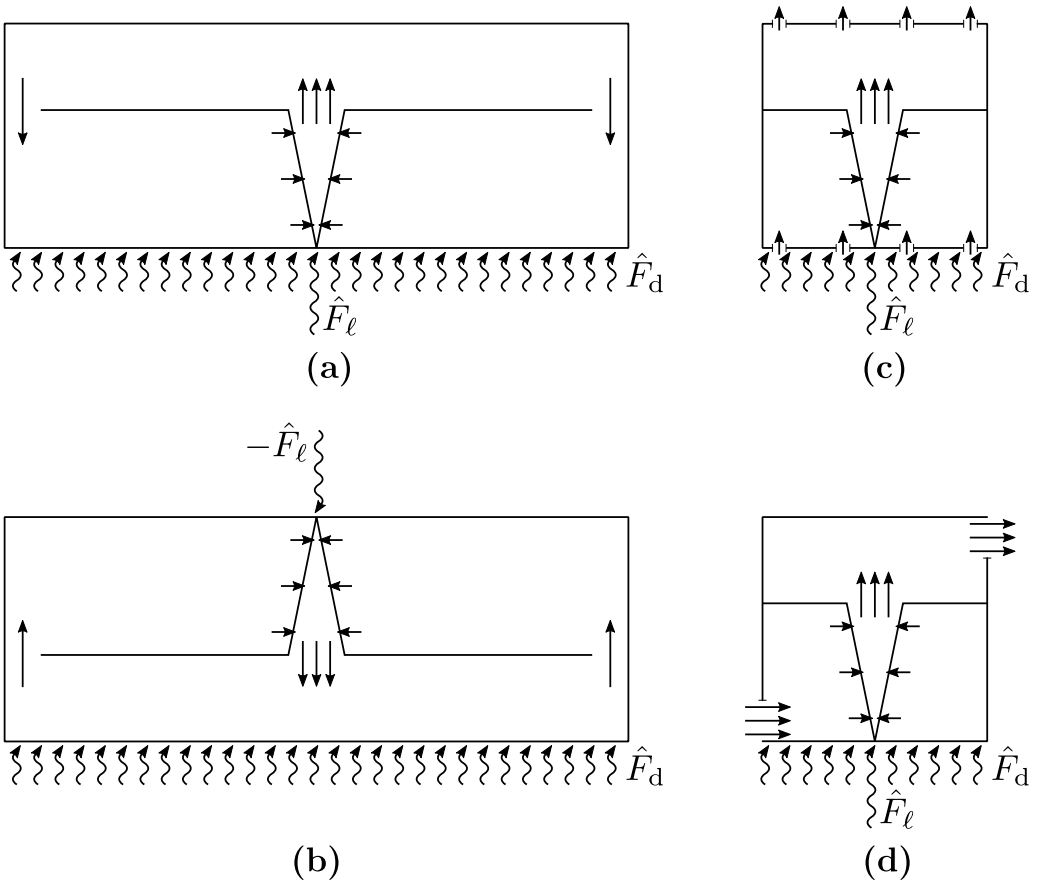

FIG. 1. Combined localized ($\hat{F}_\ell$) and distributed ($\hat{F}_\mathrm{d}$) buoyancy sources investigated in the literature ($\hat{F}_\ell, \hat{F}_\mathrm{d} > 0$). Depicted are the configurations for confined volume heating from Wells, Griffiths, and Turner [10], using sources on (a) the same and (b) opposite boundaries. Also sketched are the configurations for the heating of a ventilated domain as considered by (c) Chenvidyakarn and Woods [11] (based on textual description) and (d) Hunt, Holford, and Linden [12] and Partridge and Linden [13].

Distributed heat sources produce flows and stratifications that are markedly different from those produced by localized heat sources. An example is Rayleigh-Bénard convection [9], which is characterized by vigorous turbulence throughout the domain that homogenizes the buoyancy field and thus suppresses the emergence of stably stratified layers (note, however, that the flow can organize into large-scale patterns or "wind" which cause spatial heterogeneity). The combination of localized and distributed sources of heat, and therefore buoyancy, leads to a competition between the stabilizing effect of the localized source, and the destabilizing effect of the distributed source [10].

Despite their prevalence in realistic settings, cases of combined localized and distributed heating have received relatively little attention. The combination of a single localized point source and a distributed source in a closed domain was investigated experimentally by Wells, Griffiths, and Turner [10] [Figs. 1(a) and 1(b)]. They found that the stable stratification created by the plume breaks down when the buoyancy flux from the distributed source $\hat{F}_\mathrm{d}$ exceeds that of the plume, $\hat{F}_\ell$. Work by Chenvidyakarn and Woods [11], Partridge and Linden [13], and Hunt, Holford, and Linden [12] in this regard focused on open domains that support inflow and outflow through the bottom and top of the domain [11] [Fig. 1(c)] or through openings in the side walls [12,13] [Fig. 1(d)].

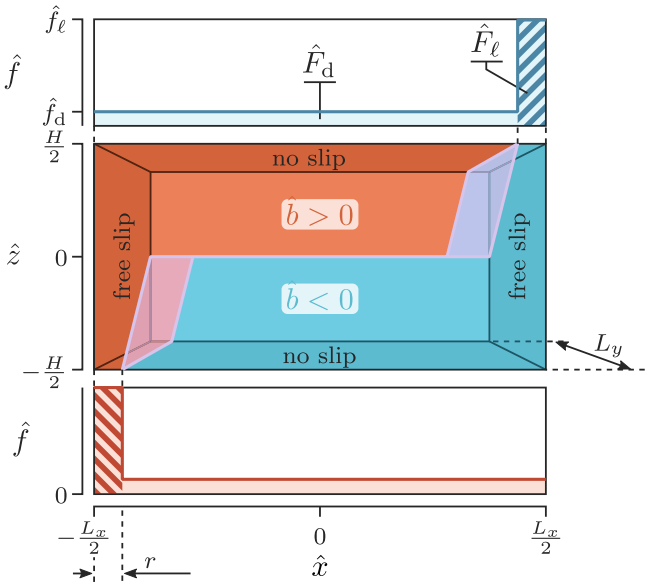

FIG. 2. Schematic of the investigated configurations. The horizontal boundaries are set to a constant local buoyancy flux $\hat{f}_\ell$ within a strip of width r; the remainder of each boundary is set to $\hat{f}_\mathrm{d}$ (top and bottom graphs). The structure of buoyancy $\hat{b}$ sketched in the middle depicts two plumes in a stable two-layer stratification.

In these cases, the volume flux or ventilation is an additional parameter on which the breakdown of the stratification depends [11,13] (Hunt, Holford, and Linden [12] describe a breakdown that is independent of the ventilation based on a set of preliminary experiments; this concept was improved by Partridge and Linden [13]). In spite of differences in their models' formulation, Chenvidyakarn and Woods [11] and Partridge and Linden [13] both report successful predictions of the system.

In this paper, we study combinations of localized and distributed heating in a closed domain. In contrast to Wells *et al.* [10], we focus on configurations involving no net heating or cooling of the domain, which therefore admit statistically steady states, even for different ratios of localized and distributed heating. This choice allows us to obtain statistics from averages with respect to time. The specific case we consider consists of heating and cooling on the bottom and top boundaries, respectively, from a combination of a localized *line* source and a distributed *area* source. The line sources on the top and bottom boundary are of equal strength, as are the area sources. Previous work has studied similar arrangements involving localized *point* sources in the absence of distributed sources [6,8].

In Sec. II, we define the problem and describe the simulations in Sec. III, before presenting results in Sec. IV. Building on the observations of Sec. IV, we construct two models of the steady state buoyancy field in Sec. V, which adopt different assumptions about the horizontal distribution of buoyancy within the domain. We compare both models with the simulation results in Sec. VI and provide conclusions in Sec. VII.

II. PROBLEM DESCRIPTION

We consider a box of width L_x, depth L_y, and height H which is heated at the bottom and cooled at the top by a combination of localized and distributed sources (Fig. 2). The origin of the coordinates in the corresponding directions, $(\hat{x}, \hat{y}, \hat{z})$, is placed at the center of the domain. The problem is statistically homogeneous in the $\hat{y}$ direction. At the vertical boundaries of the domain we impose a free-slip condition on the flow velocity and at the horizontal boundaries we impose a no-slip condition.

We study the enclosure under different distributions of boundary heating, where the total buoyancy flux $\hat{F}$ per unit width on the top and bottom boundary,

$$\hat{F} \equiv \frac{1}{L_y} \int_{-\frac{L_x}{2}}^{\frac{L_x}{2}} \int_{-\frac{L_y}{2}}^{\frac{L_y}{2}} \hat{f}(\hat{x}, \hat{z}) \Big|_{\hat{z}=\pm\frac{H}{2}} d\hat{x}\, d\hat{y}\,, \tag{1}$$

is held constant for different heating distributions. The local buoyancy flux $\hat{f}(\hat{x}, \hat{z})$ which we impose on the top and bottom boundary corresponds to a buoyancy gradient, $\hat{f}|_{\hat{z}=\pm\frac{H}{2}} = -\kappa \partial_{\hat{z}} \hat{b}|_{\hat{z}=\pm\frac{H}{2}}$, since there is no advective buoyancy transport across the boundaries. The buoyancy field $\hat{b} = g(\rho_0 - \rho)/\rho_0$ accounts for the density ρ of the fluid relative to a reference density ρ_0, where g is the absolute value of the gravitational acceleration and κ the thermal diffusivity. The buoyancy flux at the side walls is set to zero.

The total buoyancy flux $\hat{F}$ at each of the horizontal boundaries can be decomposed into a buoyancy flux $\hat{F}_\ell$ from a localized source and a buoyancy flux $\hat{F}_\mathrm{d}$ from a distributed source:

$$\hat{F} = \hat{F}_\ell + \hat{F}_\mathrm{d}\,, \tag{2}$$

where $\hat{F}_\ell > 0$ and $\hat{F}_\mathrm{d} > 0$ assume the same values on the top and bottom boundary of the domain (Fig. 2). The localized sources are line sources, realized as strips of width r, and result in a pair of oppositely oriented planar plumes (Fig. 2). Distributed heating is included by setting the remaining area of the horizontal boundaries to have the buoyancy flux $\hat{F}_\mathrm{d}$. We consider the case of purely localized heating ($\hat{F}_\mathrm{d} = 0$) as the base case and investigate the flow and stratification for increasing values of the distributed heat flux $\hat{F}_\mathrm{d} > 0$.

The sources corresponding to $\hat{F}_\ell$ and $\hat{F}_\mathrm{d}$ are heated or cooled uniformly, such that the respective local buoyancy fluxes $\hat{f}_\ell$ and $\hat{f}_\mathrm{d}$ are constants (Fig. 2). We only consider cases with $\hat{f}_\ell \geqslant \hat{f}_\mathrm{d}$. Noting the planar geometry of the problem, the quantities $\hat{F}$, $\hat{F}_\ell$, and $\hat{F}_\mathrm{d}$ are defined as buoyancy fluxes per unit length, which we refer to as buoyancy fluxes for brevity. Equivalent terminology will be applied to the the volume and momentum flux.

A combination of localized and distributed heating can result in a stable stratification into two layers [10] at a buoyancy difference $\Delta\hat{b}$ (Fig. 2). The buoyancy difference is determined by the geometry of the domain, L_x, L_y, H, the strip width r, the buoyancy fluxes $\hat{F}_\ell$ and $\hat{F}_\mathrm{d}$ on the boundaries and the fluid's properties, the kinematic viscosity ν, and thermal diffusivity κ. Using H and $\hat{F}$ to nondimensionalize the problem, the dimensionless buoyancy difference $\Delta b = \Delta\hat{b}\, H\, \hat{F}^{-\frac{2}{3}}$ becomes a function of six dimensionless characteristic parameters

$$\Delta b \;=\; h(\,\lambda,\; \Lambda,\; \Lambda_y,\; \mathrm{Re},\; \mathrm{Pr},\; \Gamma\,), \tag{3}$$

where

$$\lambda = \frac{r}{L_x}, \quad \Lambda = \frac{L_x}{H}, \quad \Lambda_y = \frac{L_y}{H}, \quad \mathrm{Re} = \frac{H\,\hat{F}^{\frac{1}{3}}}{\nu}, \quad \mathrm{Pr} = \frac{\nu}{\kappa}, \quad \Gamma = \frac{\hat{F}_\mathrm{d}}{\hat{F}_\ell}. \tag{4}$$

The quantities λ, Λ, and Λ_y are the aspect ratio of the plume source and the aspect ratios of the domain's width and depth, respectively, and therefore capture the geometry of the domain. Here, an ideal line source of infinitesimal width corresponds to $\lambda = 0$. The Reynolds number Re is defined independently of the distribution of the buoyancy flux on the boundary and Pr is the Prandtl number. The ratio Γ of the distributed to the localized buoyancy flux measures the distribution of the buoyancy flux on the boundaries. Due to the restrictions placed on $\hat{F}_\ell$ and $\hat{F}_\mathrm{d}$, the buoyancy flux ratio in this problem is limited to $\Gamma \geqslant 0$. The buoyancy flux ratio $\Gamma = 0$ corresponds to the case of localized sources in an insulated boundary, whereas for Rayleigh-Bénard convection its value is $\Gamma = \lambda^{-1} - 1$. If the localized source was a line source of infinitesimal width, the latter value would be independent of the line source width λ and $\Gamma \to \infty$ for Rayleigh-Bénard convection.

From (2) and (4), the dimensionless counterparts of $\hat{F}_\ell$ and $\hat{F}_\mathrm{d}$ are

$$F_\ell \equiv \frac{\hat{F}_\ell}{\hat{F}} = \frac{1}{1+\Gamma}, \quad F_\mathrm{d} \equiv \frac{\hat{F}_\mathrm{d}}{\hat{F}} = \frac{\Gamma}{1+\Gamma}, \tag{5}$$

such that $F_\ell + F_\mathrm{d} = 1$. The dimensionless local buoyancy fluxes are termed f_ℓ and f_d.

To maximize the distance between the plumes without introducing the additional complications associated with no-slip boundary conditions, we use free-slip boundary conditions on the vertical walls. However, a plume at such a wall should not be regarded as half of an unconfined plume, because the impenetrable wall limits the scale of cross-stream turbulent motion and reduces entrainment, nor does it represent an experimentally observable wall-bounded plume, due to the lacking wall-shear stress (for details, see Appendix A).

III. SIMULATION DETAILS

The configurations introduced in Sec. II were investigated using direct numerical simulations (DNS). To study the effect of the heating distribution, all characteristic parameters of the problem were kept constant apart from the buoyancy flux ratio Γ. Simulations were run for different values of the buoyancy flux ratio, ranging from the case of purely localized heating, $\Gamma = 0$, to a configuration for which the distributed contribution to the buoyancy flux on the boundary exceeds the localized one, $\Gamma > 1$.

The nondimensional governing equations are those of an incompressible fluid under the Boussinesq approximation:

$$\nabla \cdot \mathbf{u} = 0, \tag{6a}$$

$$\partial_t \mathbf{u} + (\mathbf{u}\cdot\nabla)\mathbf{u} = -\nabla p + \mathrm{Re}^{-1}\Delta\mathbf{u} + b\,\mathbf{e}_z, \tag{6b}$$

$$\partial_t b + \mathbf{u}\cdot\nabla b = \mathrm{Pe}^{-1}\Delta b, \tag{6c}$$

where $\mathbf{u}$, p, and b correspond to the velocity vector, the kinematic pressure, and the buoyancy, respectively; $\mathrm{Pe} = \mathrm{Pr}\,\mathrm{Re}$ is the Péclet number. The scales used to nondimensionalize space $\mathbf{x}$, time t, velocity, pressure, and buoyancy are H, $H\,\hat{F}^{-\frac{1}{3}}$, $\hat{F}^{\frac{1}{3}}$, $\hat{F}^{\frac{2}{3}}$, and $H^{-1}\,\hat{F}^{\frac{2}{3}}$, respectively.

The Prandtl number was chosen as that of air, $\mathrm{Pr} = 0.7$, and the Reynolds number is $\mathrm{Re} = 7.34 \times 10^3$, corresponding to a Rayleigh number $\mathrm{Ra} = \mathrm{Pr}\,\mathrm{Re}^2 = 3.77 \times 10^7$. The buoyancy flux ratio Γ on the boundary takes the values $\Gamma \in \{0,\ 0.10,\ 0.23,\ 0.39,\ 0.60,\ 1.29\}$. The governing equations (6) were solved on a domain of aspect ratios $\Lambda = 2$ and $\Lambda_y = \frac{3}{2}$, discretized as a staggered equidistant Cartesian grid of $1024 \times 768 \times 512$ cells. The resulting grid spacing, $\Delta x = 2 \times 10^{-3}$, is appropriate for the Kolmogorov length $\eta_\mathrm{Kol} \sim \mathrm{Pr}^{\frac{3}{8}}\,\mathrm{Ra}^{-\frac{3}{8}} = 1.26 \times 10^{-3}$. The initial volume integrated buoyancy of the domain is zero.

The DNS were performed using the code SPARKLE [14], which is based on finite volume discretization. The central differencing scheme employed is the fourth-order symmetry-preserving method of Verstappen and Veldman [15]. Time integration was performed using a second order Adams-Bashford scheme with adaptive time stepping. For further details about the code, see Craske and van Reeuwijk [14]. A line source of width $\lambda = \frac{1}{16}$ was found to be sufficiently small to produce a planar plume (see Appendix A). To initiate turbulent plumes [16], we add 1% of white noise to the vertical velocity on a single horizontal layer of grid points adjoining the source areas.

We define the mean of a field $h(t, x, y, z)$ over the homogeneous y direction and time as

$$\overline{h}(x,z) = \frac{1}{T\,\Lambda_y}\int_0^T \int_{-\frac{\Lambda_y}{2}}^{\frac{\Lambda_y}{2}} h(t,x,y,z)\,dy\,dt \tag{7}$$

and $h' = h - \overline{h}$ as the corresponding fluctuation. Statistics are taken at the steady state over $T = 10$ dimensionless turnover times, where the turnover time is one unit of nondimensional time consistent with (6). Due to the symmetry of the boundary conditions, the mean fields of the Reynolds averaged

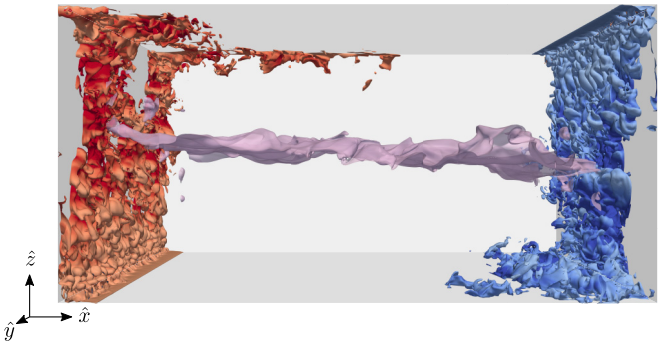

FIG. 3. Isopycnals of two oppositely oriented plumes, arising from two localized line sources of equal strength ($\Gamma = 0$). Red marks an isosurface at buoyancy $b \approx 5$, blue corresponds to $b \approx -5$; the color saturation indicates the kinetic energy. The fluid in the bulk of the domain is stably stratified in two layers, which are separated by an interface of zero buoyancy (violet). The displayed isosurface of zero buoyancy is cropped at the boundaries so as not to obscure the plumes.

governing equations are (anti-)symmetric to the axis $(x, z) = (0, 0)$ in the steady state. We exploit this property when taking statistics, such that the resulting mean fields obey these symmetries exactly.

Using a Reynolds decomposition and integrating (6c) over the width Λ of the domain, we obtain the following relation for F, the mean buoyancy flux over a horizontal slice:

$$\partial_z F \;\equiv\; \partial_z \int_{-\frac{\Lambda}{2}}^{\frac{\Lambda}{2}} (\overline{w}\,\overline{b} + \overline{w'\,b'} - \mathrm{Pe}^{-1}\,\partial_z \overline{b})\,dx \;=\; 0. \tag{8}$$

Thus, the mean buoyancy flux F is conserved in z. This relation is utilized to determine whether the steady state is reached; we consider a state as statistically steady if the standard deviation of the buoyancy flux F, with respect to the unit buoyancy flux at the top or bottom boundary, is less than a given critical standard deviation $\sigma_c = 10^{-2}$.

Depending on the buoyancy flux ratio Γ, one turnover time took between 4.4×10^3 and 7.4×10^3 core hours to compute.

IV. RESULTS

A. Buoyancy structure

Heating and cooling the domain via two localized line sources of buoyancy on an otherwise insulated boundary ($\Gamma = 0$) leads to a stable stratification, consisting of two layers of near-uniform buoyancy [Figs. 3 and 4(a)]. The line sources produce two oppositely oriented turbulent planar plumes. Each plume supplies one layer of the resulting stable two-layer stratification by entraining fluid from its ambient layer and discharging into the opposite layer. The two layers are separated by an interface which has zero buoyancy, since the buoyancy sources on the top and bottom boundary are of equal strength and the initial volume integrated buoyancy of the domain is zero. The mean buoyancy $\overline{b}(x, z)$ of the domain, shown representatively at $x = 0$ in Fig. 6, is characterized by a weak stratification in each layer and a thin transitional layer with a high buoyancy gradient at the interface.

The two-layer stratification at $\Gamma = 0$ [Fig. 4(a)] manifests as two distinct peaks in the time-averaged probability density function (PDF) of the buoyancy field (Fig. 5). The approximate uniformity of the buoyancy field in each of the layers is evident from the narrow width of the PDF peaks. The uniformly low value of the PDF between the peaks corresponds to the sharp separation of the two layers, resulting in the distinct interface visible in Fig. 4(a).

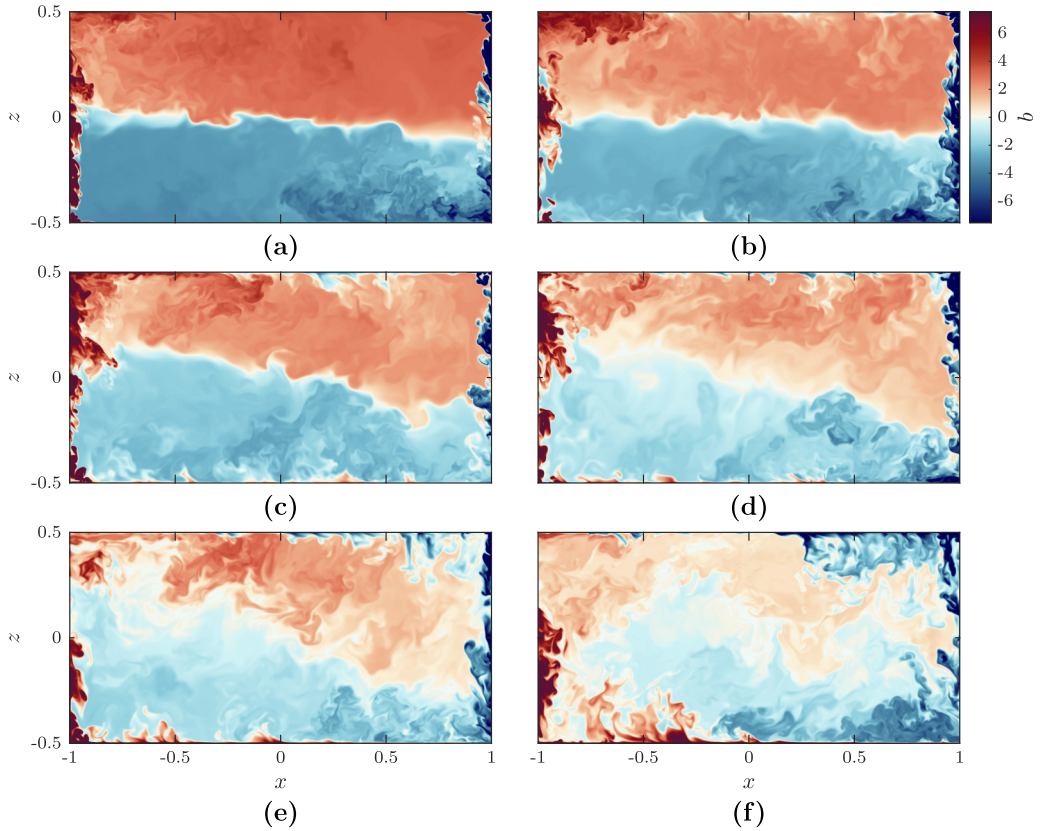

FIG. 4. Instances of the buoyancy field: the individual figures correspond to (a) $\Gamma = 0$, (b) $\Gamma = 0.10$, (c) $\Gamma = 0.23$, (d) $\Gamma = 0.39$, (e) $\Gamma = 0.60$, and (f) $\Gamma = 1.29$.

When a distributed buoyancy flux is added to the boundary ($\Gamma > 0$), the buoyancy difference between the layers decreases (Fig. 6), which means that the distance between the peaks of the PDF in Fig. 5 decreases. This trend continues as the value of Γ increases, until the two-layer stratification breaks down for $0.60 < \Gamma < 1.29$ [Figs. 4(e) and 4(f)]. The transition is evident from the PDF, as the two peaks of $\Gamma < 1.29$ merge into a single peak at $\Gamma = 1.29$ (Fig. 5). This behavior is in agreement

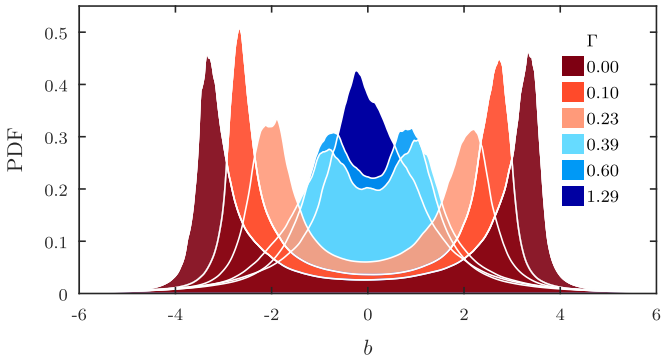

FIG. 5. Time-averaged probability density function of the buoyancy field.

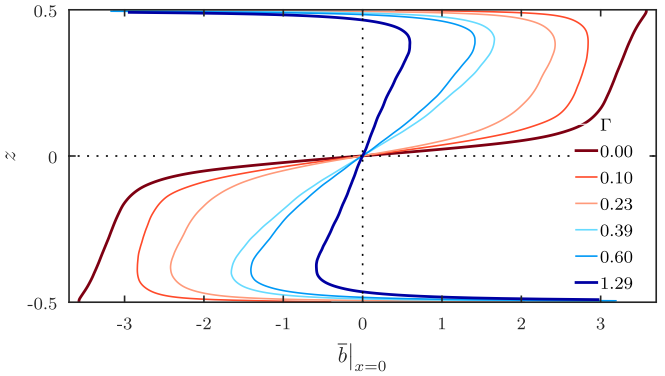

FIG. 6. Mean buoyancy $\overline{b}$ along a vertical slice in the middle of the domain ($x = 0$). At the chosen position $x = 0$, the interface elevation is $z = 0$ for all configurations.

with the breakdown of the stable stratification for $\Gamma > 1$ reported by Wells, Griffiths, and Turner [10]. The experimental configurations of Wells *et al.* are similar to the ones investigated here, if one localized and one distributed source were removed from the latter [Figs. 1(a), 1(b), and 2]. The correlation with Wells *et al.* suggests $\Gamma = 1$ as the critical value for the breakdown of the two-layer stratification in the configurations considered in the present paper.

As Γ increases from 0 to 0.60, the buoyancy field of each layer of the stable stratification decreases in homogeneity: the individual peaks in the PDF increase in width and decrease in amplitude (Fig. 5). The interface between the upper and lower layer of the stratification in Fig. 4 appears less distinct as Γ increases and the gradient of the mean buoyancy between the layers decreases (Fig. 6).

Between $\Gamma = 0.23$ and 0.39, the buoyancy difference between the layers decreases abruptly and then shrinks only marginally as Γ increases to 0.60. The abrupt decrease of the buoyancy difference between the layers is accompanied by a marked increase in the heterogeneity of the buoyancy field in each layer, which is reflected in the width of the PDF peaks. The increase in the amplitude of the peaks in the PDFs for $\Gamma \geqslant 0.39$ results from the growing overlap between the formerly distinct peaks. The vertical gradient of the mean buoyancy in each layer, which is small for $\Gamma \leqslant 0.23$, is markedly increased for $\Gamma \geqslant 0.39$ and becomes comparable in magnitude to the mean buoyancy gradient at the interface (Fig. 6).

B. Flow structure

We first consider the flow at $\Gamma = 0$. Each of the localized sources produces a turbulent plume, which entrains fluid from its environment, i.e., its adjoining buoyancy layer. Each plume discharges fluid into the layer above (or below), which corresponds to the environment from which the oppositely oriented plume entrains fluid. As a result, a large-scale circulation develops, which transports fluid between the layers via the plumes and spans the width of the domain [Fig. 7(a)].

For simplicity of expression, we will now limit our considerations to the left-hand plume and the upper layer. The flow in the plume is driven by the buoyancy of the plume's fluid relative to the local ambient fluid. As the plume penetrates the interface between the two layers of the stratification (solid red line in Fig.[7]), the mean buoyancy difference between the plume and its ambient becomes approximately zero (see Appendix A). Since the plume represents the only buoyancy source to the layer into which it is discharging, the mean buoyancy of the upper layer is approximately equal to the mean buoyancy of the plume where it penetrates the interface [6]. Thus, the plume is replaced in the upper layer by a flow that is akin to a jet in the statistical average (see Appendix A for details). The entrainment of fluid into the jet drives a secondary circulation cell, nested into the large-scale

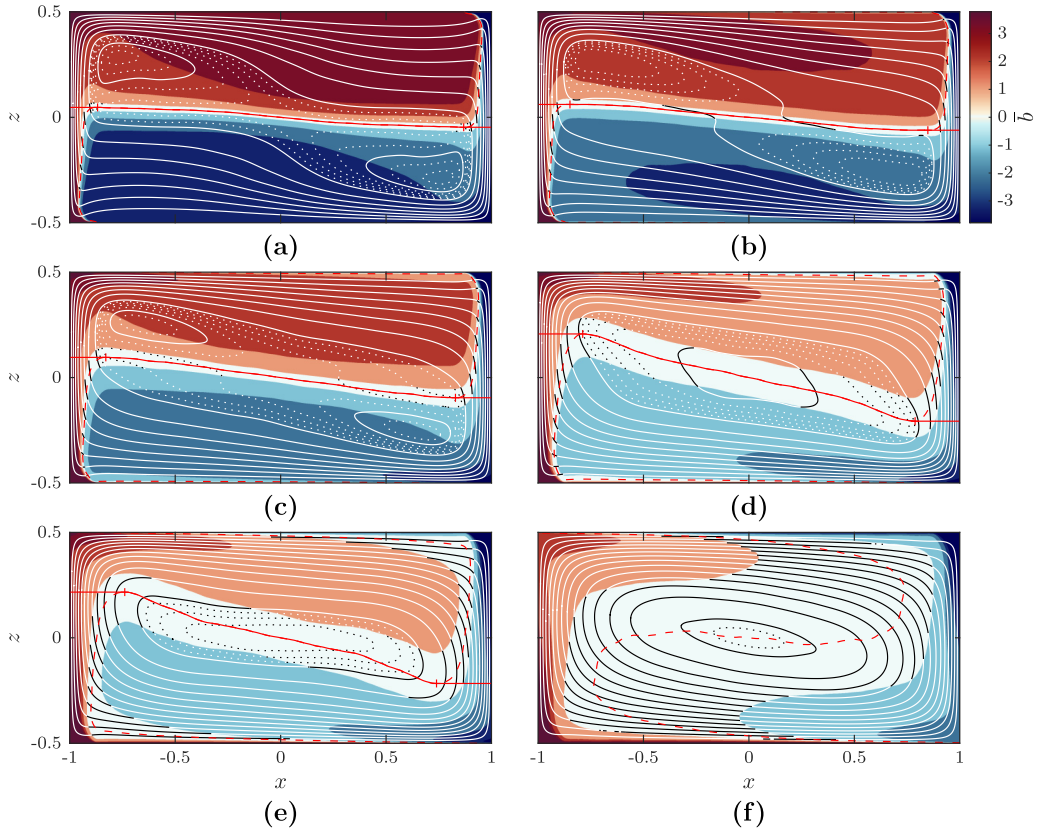

FIG. 7. Mean buoyancy field $\overline{b}$ and stream lines of the mean flow $\overline{\mathbf{u}}$: the individual figures correspond to (a) $\Gamma = 0$, (b) $\Gamma = 0.10$, (c) $\Gamma = 0.23$, (d) $\Gamma = 0.39$, (e) $\Gamma = 0.60$, and (f) $\Gamma = 1.29$. Dotted streamlines correspond to a finer scaling than solid ones, marking a fifth of the difference between the solid streamlines. The isosurface at buoyancy $b = 0$ is marked by a red dashed line; the interface between the layers and its horizontal continuation to the boundaries is marked by a solid red line. The interface is separated from the continuation by a "+." For definitions of the interface and the "+" markers, see Appendix B.

circulation, as observed by Craske and Davies Wykes [8], albeit for slightly different boundary conditions. The secondary circulation is confined to the upper layer.

The interface between two layers tilts with increasing Γ in the rotational direction of the global circulation. Consequently, the vertical extent of the jet in the upper layer decreases. The horizontal spread of the jet increases with Γ, since the width of the plume at the interface height increases with Γ. At $\Gamma = 0.39$, the depth of the upper layer on the left-hand side is comparable to the width of the plume where it penetrates the interface and the secondary circulation cells disappear [Fig. 7(d)]. The collapse of the secondary circulations at $\Gamma = 0.39$ coincides with an abrupt increase of the buoyancy field's heterogeneity in each layer (Sec. IV A). The observed change in the vertical distribution of the mean buoyancy (Sec. IV A) also appears to be connected to the secondary circulations. The mean buoyancy profile, which is characterized by near-uniform values in each layer and a high interfacial gradient in the presence of the secondary circulation cells ($\Gamma \leqslant 0.23$), takes on an approximately constant vertical buoyancy gradient in the bulk as the secondary circulations disappear ($\Gamma \geqslant 0.39$, Fig. 6).

Increasing Γ beyond $\Gamma = 0.39$, the interface tilts further, until the stable stratification breaks down at $\Gamma = 1.29$ [Fig. 7(d)] and the isosurface $\overline{b} = 0$ returns to a near-horizontal orientation in the

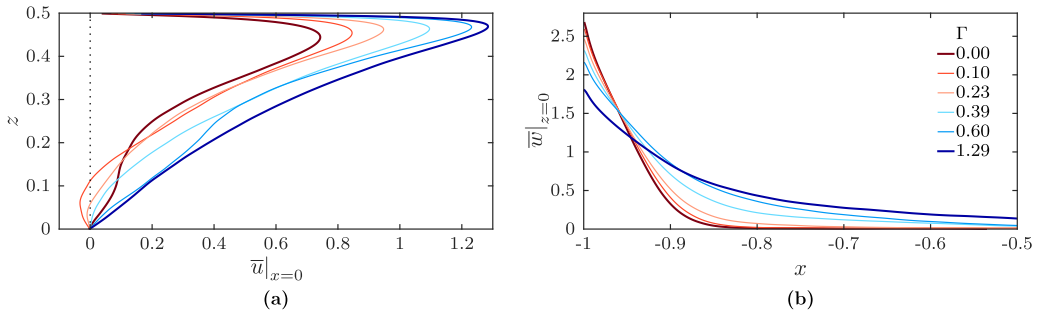

FIG. 8. Profiles of mean velocities: (a) the horizontal velocity $\overline{u}$ along a vertical slice in the middle of the domain ($x = 0$) and (b) the mean vertical velocity $\overline{w}$ in the left-hand plume at $z = 0$. At the position $x = 0$ depicted in (a), the interface elevation is $z = 0$ for all configurations and the mean velocity is antisymmetric to $z = 0$, $\overline{u}(0, z) = -\overline{u}(0, -z)$.

bulk. The flow retains a large-scale circulation, where the direction of rotation is determined by the localized buoyancy sources. If Γ was increased further, we would expect a Rayleigh-Bénard-like flow, where the bias of the flow orientation disappears (at least in an ensemble-averaged manner [17]), although it is potentially susceptible to spontaneous change [18]. We therefore expect the buoyancy distribution in the vertical to continue the trend visible in Fig. 6 and reach a near-uniform buoyancy value in the bulk.

The slice of the mean buoyancy field in Fig. 6 was placed at $x = 0$ because at this position the interface is conveniently at a constant elevation $z = 0$ for all Γ. The buoyancy in the layers is, however, not uniform in x. A fluid parcel in the upper layer is gradually cooled by the top boundary's buoyancy flux as it is transported from left to right. Consequently, the distributed heating in conjunction with a large-scale circulation results in a lateral buoyancy gradient within the layer, where the gradient increases with Γ (Fig. 7). This lateral gradient will be the subject of further analysis in Sec. V.

The value of the mean lateral velocity $\overline{u}$ in each layer peaks close to the horizontal boundary and its highest absolute value increases with Γ [Fig. 8(a)]. Close to the interface [$z = 0$ in Fig. 8(a)], the behavior of $\overline{u}$ appears to be nonmonotonic with Γ for small values of Γ. This is a result of the changing width of the secondary circulation cells: at $\Gamma = 0$, the slice $x = 0$ does not intersect the secondary circulation, but does so at $\Gamma \in \{0.10, 0.23\}$, leading to different curves $\overline{u}(0, z)$ close to the interface. Figure 8(a) implies that the volume flux of the primary circulation increases with Γ, since the horizontal velocity component dominates the mean flow at $x = 0$. Thus, we observe a larger volume flux when the bias of the localized sources on the flow orientation is reduced. However, our observations concern configurations where a two-layer stratification persists; the effect of localized sources on the volume flux for $\Gamma > 1$ might differ.

The value of the mean vertical velocity $\overline{w}$ in the plumes peaks at the side walls, where a free-slip condition is imposed [Fig. 8(b)]. The peak value of $\overline{w}$ at $z = 0$ decreases with increasing Γ, that is, with diminishing strength of the localized sources $F_\ell = (1 + \Gamma)^{-1}$. In contrast, the volume flux of $\overline{w}(x, 0)$ in Fig. 8(b) should increase with Γ, since the volume fluxes corresponding to the velocities of Figs. 8(a) and 8(b) are approximately equal for $\Gamma \leqslant 0.60$. This is because the mean velocity field is dominated by the vertical component $\overline{w}$ at $z = 0$ and by the horizontal component $\overline{u}$ at $x = 0$ and because the mean flow across the interface between the layers is weak for $\Gamma \leqslant 0.60$ (Fig. 7). The opposite trends of volume flux and peak velocity in Fig. 8(b) are possible, since the spatial distribution of $\overline{w}(x, 0)$ spreads in the horizontal with increasing Γ. The increase of the volume flux with Γ will be shown rigorously in Sec. VI C.

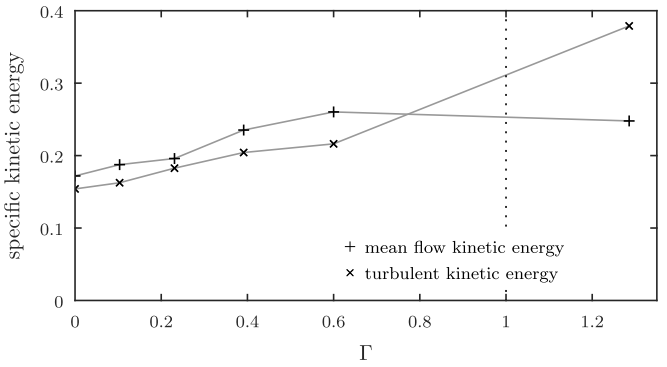

FIG. 9. Mean flow and turbulent contribution to the specific kinetic energy in the domain.

The specific kinetic energy of the flow,

$$E_{\mathrm{k}} = \frac{1}{2\,\Lambda} \int_{-\frac{\Lambda}{2}}^{\frac{\Lambda}{2}} \int_{-\frac{1}{2}}^{\frac{1}{2}} (|\overline{\mathbf{u}}|^2 + \overline{|\mathbf{u}'|^2}) dz\, dx, \tag{9}$$

consists of a mean and a turbulent contribution, corresponding to the first and second term in the above expression, respectively. The turbulent kinetic energy increases with Γ (Fig. 9), particularly at the transition from a stable ($\Gamma \leqslant 0.60$) to an unstable stratification ($\Gamma = 1.29$). The mean flow contribution to the kinetic energy increases with Γ while the two-layer stratification persists, but decreases slightly as the two-layer stratification breaks down. This decrease is consistent with the flow that we anticipate for a further increased value of Γ: because of the the spontaneous reversal of direction occurring in the large-scale circulation of Rayleigh-Bénard convection [18], the mean flow velocity and associated kinetic energy should tend towards zero for $\Gamma \to \infty$ (for sufficiently long time averages).

C. Buoyancy transport between the layers

For $\Gamma \leqslant 0.60$, the buoyancy field is stably stratified in two layers, each supplied by a plume. The layers are separated by the isosurface of zero buoyancy, which also envelops the plumes (red dashed lines in Fig. 7). For a precise definition of the two layers, we introduce a separating curve s which stretches over the full width of the domain (red solid lines in Fig. 7). The curve s coincides with $\overline{b} = 0$ in the bulk and is continued to the left and right boundary by a horizontal line (see Appendix B); the points where it departs from the isosurface are marked by red "+" markers in Fig. 7.

Buoyancy exchanged between the two layers is either transported across the interface, defined as s between the "+" markers, or via the plumes, i.e., across the two horizontal segments of s between the markers and the boundaries. We denote the buoyancy fluxes across the interface and the plumes as F_{I} and F_{p}, respectively (for a formal definition, see Appendix B). In the steady state, the mean total buoyancy flux between the layers should equal the total buoyancy flux across the horizontal boundaries of the enclosure, $2\,F_{\mathrm{p}} + F_{\mathrm{I}} = 1$. This equality holds to within an accuracy of 1% for all simulations $\Gamma \leqslant 0.60$. The simulation at $\Gamma = 1.29$ is excluded, since the buoyancy field does not show a clear two-layer stratification in this case.

Figure 10 shows that the buoyancy transport between the layers is dominated by the plumes in all simulations $\Gamma \leqslant 0.60$. The value of the plumes' buoyancy flux F_{p} is unaffected by the distribution of the buoyancy flux on the boundary Γ. Splitting the buoyancy flux of the plume into a turbulent buoyancy flux and a contribution of the mean flow (Fig. 10), we find that the latter accounts for approximately 70% of the total F_{p} in the case of purely localized heating ($\Gamma = 0$). This is in agreement with experimental observations of planar plumes [19]. As Γ increases, the flow becomes

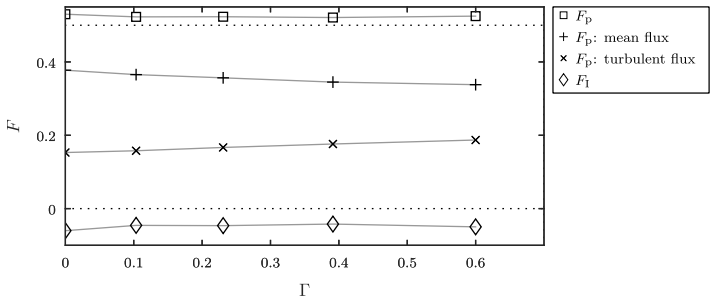

FIG. 10. Buoyancy exchange between the two layers of the stable stratification (i.e., across the red solid lines in Fig. 7). Depicted are the buoyancy fluxes F_p and F_l, corresponding to the discharge of one plume and mixing across the interface, respectively. In case of F_p, the total, the mean flow, and the turbulent contribution are depicted.

increasingly turbulent (Sec. IV B) and the turbulent buoyancy flux of the plume rises slightly, which is accompanied by a corresponding decrease in the mean flow contribution (Fig. 10).

The buoyancy flux of each plume is slightly above 0.5. Thus, the equality $1 = 2\,F_p + F_l$ is balanced by a negative buoyancy flux F_l across the interface due to turbulent mixing. The cross-interface buoyancy transport in the steady state has been studied by Chenvidyakarn and Woods [11] and Partridge and Linden [13] for other configurations of combined localized and distributed heating (Fig. 1). Chenvidyakarn and Woods find a value of $F_l \approx 0.1\,F_d$, whereas Partridge and Linden observe no mean buoyancy transport across the interface. Our results show a buoyancy flux of interfacial mixing that is negligibly small for all simulations $\Gamma \leqslant 0.60$, at about 5% of the total buoyancy flux of the boundaries. We did not observe a correlation between the value of the distributed buoyancy flux F_d and the cross-interface buoyancy flux F_l.

In spite of the Γ-independent and negligible value of F_l, the turbulent kinetic energy increases with Γ (Fig. 9). Indeed, the behavior of the turbulent kinetic energy might suggest an increase of the cross-interface buoyancy flux F_l with Γ, due to increased interfacial mixing. However, any increase of F_l would be counteracted by the behavior of the buoyancy difference Δb between the layers of the stratification. The value of Δb decreases more rapidly with Γ than the turbulent kinetic energy rises with Γ (compare Figs. 12 and 9). Thus, a constant buoyancy flux across the interface can be consistent with a turbulent kinetic energy increasing with Γ.

V. MODELING THE BUOYANCY FIELD

We develop two models of the stably stratified buoyancy field found in a steady state using volume and buoyancy conservation. The models are defined in a piecewise manner; they each consist of four parts that correspond to the two plumes and the layers of the two-layer stratification (Fig. 11). Model 1 uses a simple buoyancy structure by assuming that the buoyancy in each of the stratified layers is uniform. Model 2 includes a lateral buoyancy gradient in the layers and admits a tilt of the interface between the layers.

A. Model 1

We assume that each of the two layers of the stratification is well mixed and thus model the buoyancy of the layers, $\pm b_a$, as uniform in x and z [Fig. 11(a)]. Due to the symmetry of the problem, the buoyancy of the two layers differs in sign only and it is sufficient to consider a single layer with its adjoining plumes. For the purpose of discussion, we will therefore focus on the upper layer of buoyancy b_a.

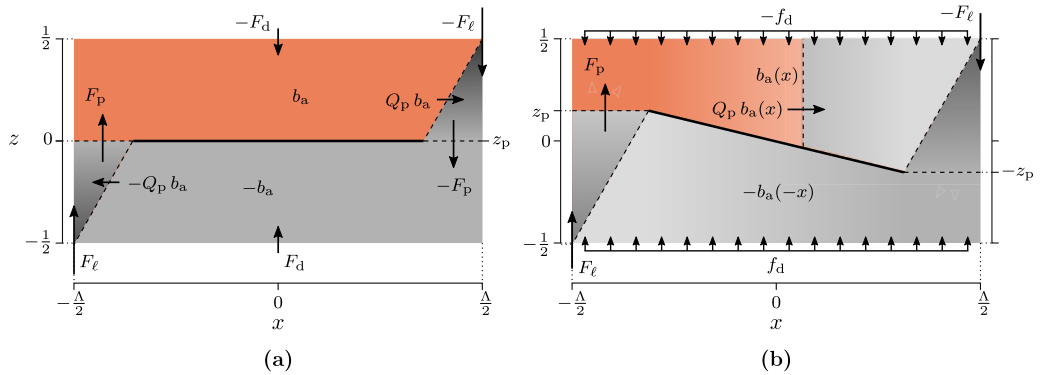

FIG. 11. Schematics of the buoyancy structure for the models of (a) Sec. V A and (b) Sec. V B. The highlighted section is the control volume used. The volume flux across all dashed boundaries is equal Q_p.

The upper layer is supplied by the left-hand plume with a mean buoyancy flux F_p. The top boundary of buoyancy flux F_d and the entraining right-hand plume act as buoyancy sinks. Consistent with Sec. IV C, we neglect the buoyancy transport across the interface between the layers ($F_\mathrm{I} = 0$) and hence set $F_\mathrm{p} = \frac{1}{2}$ (see Sec. IV C). In the steady state, the volume flux associated with entrainment into the right-hand plume equals the volume flux Q_p of the left-hand plume at the interface. Thus, we model the buoyancy flux into the right-hand plume as $Q_\mathrm{p}\, b_\mathrm{a}$. Using Eq. (5) for F_d, the buoyancy conservation of the upper layer in the steady state yields

$$\underbrace{\frac{1}{2}}_{F_\mathrm{p}} = Q_\mathrm{p}\, b_\mathrm{a} + \underbrace{\frac{\Gamma}{1+\Gamma}}_{F_\mathrm{d}}. \tag{10}$$

A plume from a source of strength $F_\ell = (1+\Gamma)^{-1}$ placed at $z = -\frac{1}{2}$ penetrates the interface at z_p with a volume flux [20] (see Appendix A)

$$Q_\mathrm{p} = \alpha^{\frac{2}{3}}\,(1+\Gamma)^{-\frac{1}{3}}\left(z_\mathrm{p} + \tfrac{1}{2}\right), \tag{11}$$

where α is the entrainment coefficient. We model the interface between the buoyancy layers as horizontal and hence the plume height as $z_\mathrm{p} = 0$, neglecting the tilt that will be addressed in model 2 of Sec. V B.

Combining (10) and (11), we obtain the buoyancy b_a of the upper layer as $b_\mathrm{a} = \alpha^{-\frac{2}{3}}\,(1-\Gamma)\,(1+\Gamma)^{-\frac{2}{3}}$. The corresponding buoyancy difference between the upper and lower layer is

$$\Delta b \;=\; b_\mathrm{a} - (-b_\mathrm{a}) \;=\; 2\,\alpha^{-\frac{2}{3}}\,(1-\Gamma)\,(1+\Gamma)^{-\frac{2}{3}}. \tag{12}$$

Since the buoyancy is modeled as homogeneous in each layer, this difference is assumed to correspond to the difference between the peaks of the buoyancy field's PDF.

We defer discussion of the performance of the model to Sec. VI and proceed with the construction of a second model, which incorporates a horizontal variation in both the buoyancy field and interface height.

B. Model 2

For the first model, we assumed the two layers of the stratification to be of homogeneous buoyancy $\pm b_\mathrm{a}$. This results in a constant buoyancy flux $Q_\mathrm{a}\, b_\mathrm{a}$ across any vertical slice of the upper (or lower) layer, independent of its position in x. Thus, assuming layers of homogeneous buoyancy neglects the spatial distribution of the buoyancy flux F_d across the upper (and lower) boundary. For

the second model, we allow the buoyancy in each layer to vary in x, but continue to assume the buoyancy layers to be well mixed over their smaller vertical dimension. The buoyancy of the upper layer at x is denoted as $b_a(x)$. Due to the antisymmetry of the buoyancy field, the buoyancy of the lower layer at position x equals $-b_a(-x)$.

We choose a segment of the upper layer as the control volume, stretching from the left-hand wall to an arbitrary position x [Fig. 11(b)]. The buoyancy flux across the top boundary in this segment is the integral of the boundary's constant local buoyancy flux, $f_d = F_d\,\Lambda^{-1}$, over the respective interval:

$$\int_{-\frac{\Lambda}{2}}^{x} f_d\,dx = F_d\left(\frac{x}{\Lambda}+\frac{1}{2}\right). \tag{13}$$

Similarly to Sec. V A, the buoyancy flux at x is modeled as $Q_p\,b_a(x)$. The volume flux Q_p is given by (11) and dependent on z_p. Combining these relations, the buoyancy conservation of the segment in the steady state gives

$$\underbrace{\frac{1}{2}}_{F_p} = Q_p\,b_a(x) + \underbrace{\frac{\Gamma}{1+\Gamma}}_{F_d}\left(\frac{x}{\Lambda}+\frac{1}{2}\right), \quad x\in\left[-\frac{\Lambda}{2},\frac{\Lambda}{2}\right]. \tag{14}$$

In the construction of this model, we neglect the horizontal spatial extent of the right-hand plume and its source, assuming that the upper layer stretches from $-\frac{\Lambda}{2}$ to $\frac{\Lambda}{2}$ for all z and that F_d is distributed uniformly over this interval.

In contrast to the first model, z_p is not necessarily equal to zero. Consistent with a laterally dependent buoyancy, we consider the vertical position of the interface between the layers as an x-dependent function $z_I(x)$. The left- and right-hand plume penetrate the interface at z_p and $-z_p$, respectively, such that $z_I(\mp\frac{\Lambda}{2}) = \pm z_p$. To obtain $z_I(x)$, we assume that the vertical velocity in the bulk is sufficiently small for the pressure to be approximated as hydrostatic [21] and is approximately constant at the top and bottom of the domain. Thus, the pressure difference between the bottom and top boundary is

$$p|_{z=-\frac{1}{2}} - p|_{z=\frac{1}{2}} = \int_{-\frac{1}{2}}^{z_I(x)} -b_a(-x)\,dz + \int_{z_I(x)}^{\frac{1}{2}} b_a(x)\,dz \tag{15}$$

$$= -Q_p^{-1}\,(1+\Gamma)^{-1}\left(z_I(x)+\Gamma\,\frac{x}{\Lambda}\right), \tag{16}$$

where we inserted b_a from (14). Due to the pressures being taken as constant in x, the above expression results in $z_I(x) = -\Gamma\,\frac{x}{\Lambda} + z_I(0)$. The offset is $z_I(0) = 0$ since $z_I(x)$ needs to be an antisymmetric function in x. Inserting $z_p = z_I(-\frac{\Lambda}{2})$ and (11) into (14), we find the buoyancy of the upper layer:

$$b_a(x) = \alpha^{-\frac{2}{3}}\,(1+\Gamma)^{-\frac{5}{3}}\left(1-\Gamma\,\frac{2x}{\Lambda}\right). \tag{17}$$

For the model, the peaks in the PDF correspond to the buoyancy over the deepest part of the layers. Thus, the buoyancy of the upper layer at $x=\frac{\Lambda}{2}$, $b_a(\frac{\Lambda}{2})$, corresponds to a peak in the buoyancy's PDF, as does the buoyancy at $x=-\frac{\Lambda}{2}$ in the lower layer, $-b_a(\frac{\Lambda}{2})$. Hence, the difference between the peaks in the buoyancy field's PDF is modeled as

$$\Delta b \;=\; b_a\left(\tfrac{\Lambda}{2}\right) - \left[-b_a\left(\tfrac{\Lambda}{2}\right)\right] \;=\; 2\,\alpha^{-\frac{2}{3}}\,(1-\Gamma)\,(1+\Gamma)^{-\frac{5}{3}}. \tag{18}$$

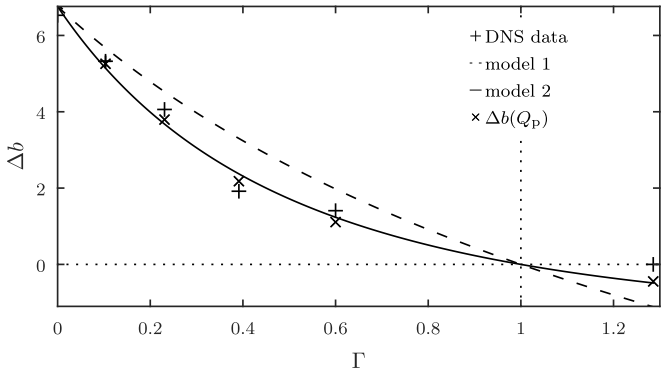

FIG. 12. Difference Δb between the peaks of the buoyancy field's PDF: comparing simulation results and models. Depicted is the buoyancy difference from simulation data (Fig. 5), and the predictions of model 1 and 2 (19). The value $\Delta b(Q_\mathrm{p})$ from (23) is a combination of modeling and observation (see Sec. VI C). The models are valid for stable stratification corresponding to $\Gamma < 1$.

VI. MODEL VERIFICATION

A. Buoyancy difference between the layers

To summarize Sec. V, the model predictions for the difference Δb between the peaks of the buoyancy field's PDF (Fig. 5) are

$$\Delta b = \begin{cases} 2\,\alpha^{-\frac{2}{3}}\,(1-\Gamma)\,(1+\Gamma)^{-\frac{2}{3}}, & \text{for } b_\mathrm{a} = \text{const} \quad \text{(model 1)}, \\ 2\,\alpha^{-\frac{2}{3}}\,(1-\Gamma)\,(1+\Gamma)^{-\frac{5}{3}}, & \text{for } b_\mathrm{a} = b_\mathrm{a}(x) \quad \text{(model 2)}. \end{cases} \tag{19}$$

As discussed in Sec. IV A, the buoyancy difference Δb is indicative of the stratification of the buoyancy field. Both models predict a stable stratification, $\Delta b > 0$, for boundary buoyancy flux ratios $\Gamma < 1$. Beyond the critical value $\Gamma_\mathrm{c} = 1$, the buoyancy difference becomes negative, corresponding to an unstable stratification. Thus, the buoyancy flux ratio Γ on the boundary takes the role of a stability parameter within the models. Since both models are based on a stably stratified buoyancy field, their validity is restricted to $\Gamma < 1$.

A critical value of $\Gamma_\mathrm{c} = 1$ is consistent with our observation of a stable stratification up to $\Gamma = 0.60$ and an unstable stratification at $\Gamma = 1.29$ (Fig. 5). Wells *et al.* [10] report the same critical value for other experimental configurations of competing localized and distributed buoyancy sources in an unventilated enclosure [Figs. 1(a) and 1(b), Sec. IV A]. To obtain numerical values from (19), we estimate the entrainment coefficient α based on the case of purely localized heating and using (11), which gives $\alpha = (2\,Q_\mathrm{p}|_{\Gamma=0})^{\frac{3}{2}} \approx 0.16$ (see Appendix A). We assume α to be independent of the buoyancy flux ratio Γ on the boundary.

Both models approximate the buoyancy difference Δb between the layers with comparable accuracy for the three lowest values of the boundary buoyancy flux ratio, $\Gamma \in \{0,\ 0.10,\ 0.23\}$ Fig. 12. In these configurations, secondary circulation cells are present and the PDF of the buoyancy field shows a near-uniform buoyancy in each of the two layers. Thus, the value of Δb is slightly overestimated by the homogeneous buoyancy model (model 1) and slightly underestimated when the lateral buoyancy gradient is based on the hydrostatic pressure at the bottom boundary (model 2).

As the secondary circulation breaks down, $\Gamma \geqslant 0.29$, the lateral buoyancy gradient in the bulk increases, and the assumption of homogeneous buoyancy layers used in model 1 is no longer suitable. In contrast, model 2 shows good agreement with the measurements, despite neglecting the marked vertical buoyancy gradient that establishes as the secondary circulation disappears (Fig. 6).

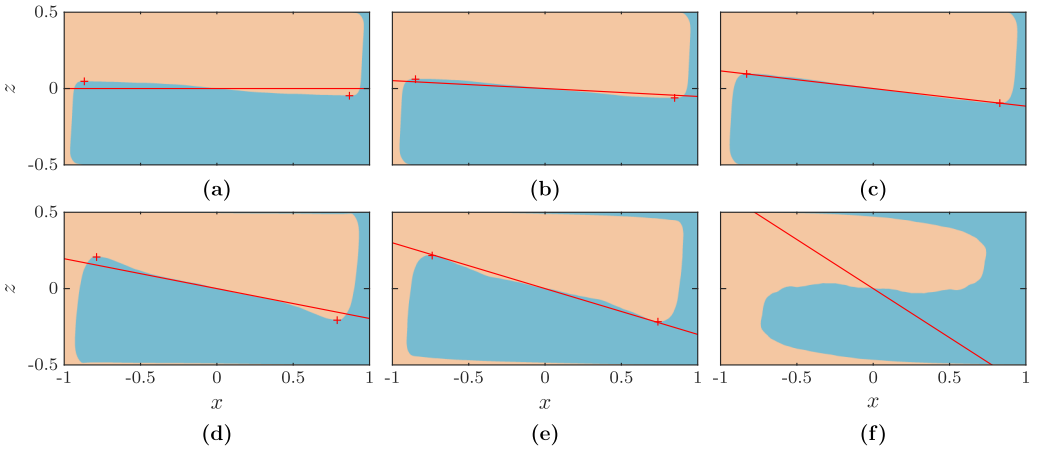

FIG. 13. Tilt of the interface between the layers of the stratification: comparing simulation results and model 2. The buoyancy field is separated into values above (red) and below (blue) zero; we consider the resulting separation line between the "+" markers as the interface (Sec. IV C). The red curve shows the interface $z_\mathrm{I}(x)$ of model 2 (Sec. V B). The individual figures correspond to (a) $\Gamma = 0$, (b) $\Gamma = 0.10$, (c) $\Gamma = 0.23$, (d) $\Gamma = 0.39$, (e) $\Gamma = 0.60$, and (f) $\Gamma = 1.29$.

B. The tilt of the interface

In Sec. V, we model the position of the interface between the layers as

$$z_\mathrm{I} = \begin{cases} 0, & \text{for model 1,} \\ -\frac{\Gamma}{\Lambda}\, x, & \text{for model 2.} \end{cases} \tag{20}$$

Using the corresponding height of the plume, $z_\mathrm{I}|_{x=-\frac{\Lambda}{2}} + \frac{1}{2}$, Δb in Eq. (19) can be written as

$$\Delta b = \alpha^{-\frac{2}{3}} \left(1 - \Gamma\right) \left(1 + \Gamma\right)^{-\frac{2}{3}} \left(z_\mathrm{I}|_{x=-\frac{\Lambda}{2}} + \tfrac{1}{2}\right)^{-1} \tag{21}$$

for both models. Thus, the difference between the two expressions in Eq. (19) originates from the different interface curves used in the models.

For $\Gamma > 0$, we find that the assumption of a hydrostatic environment and a constant pressure at the bottom boundary in model 2 (Sec. V B) lead to a tilt that is in good agreement with the interface curve defined in Sec. IV C from simulation data (Fig. 13). The upper limit $\Gamma = 1$ to the model's range of validity coincides with the interface touching the horizontal boundaries, $z_\mathrm{I}(x = \mp\frac{\Lambda}{2}) = \pm\frac{1}{2}$. Thus, the breakdown of the model beyond $\Gamma = 1$ is reflected in the interface curve [Fig. 13(f)] as well as in the buoyancy difference Δb (Sec. VI A). For $\Gamma = 0$, the model diverges slightly from the simulation data [Fig. 13(a)], predicting a horizontal interface whereas the DNS data show a tilted interface.

While the slope of the interface curve predicted by model 2 depends on the aspect ratio Λ (19), the corresponding plume height, $z_\mathrm{I}|_{x=-\frac{\Lambda}{2}} + \frac{1}{2} = \frac{1}{2}\left(1 + \Gamma\right)$, is independent of Λ. In Sec. IV B, we noted that the secondary circulations are driven by a flow that is similar to a jet in the statistical average. The vertical extent of the jet is limited by the depth remaining between the horizontal boundary and the position at which the plume penetrates the interface between the layers; the height of the jet thus decreases with a growing plume height. We therefore suspect a connection between the presence or absence of secondary circulation cells and the plume height. If this is the case, model 2 implies that the breakdown of secondary circulations is solely determined by the distribution Γ of boundary heating. The existence of secondary circulations at $\Gamma = 0$, however, is expected to depend on the aspect ratio of the domain, as is the case for confined axisymmetric plumes [8].

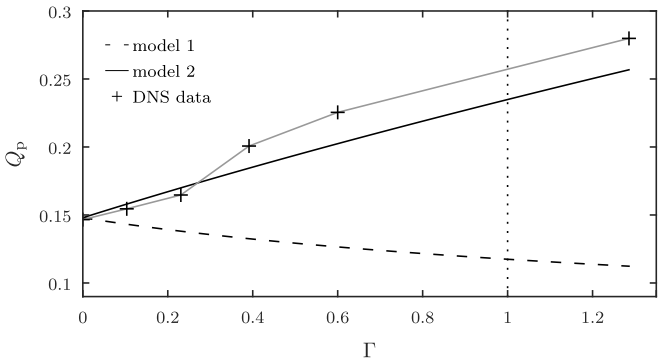

FIG. 14. Volume flux Q_p of the plume where it penetrates the interface: comparing simulation results and models. Depicted are the predictions of models 1 and 2 (23) as well as the volume flux of the plumes from simulation data. The latter is defined as the volume flux through the horizontal continuation of the interface in Fig. 7 (see Appendix B for a formal definition).

C. Volume flux

The volume flux Q_p of the plumes can be determined from the DNS data analogously to the plumes' buoyancy flux F_p in Sec. IV C: we define Q_p as an integral of the vertical velocity taken over the separating curve s between the walls and the boundaries of the interface curve marked as "+" in Fig. 7 (see Appendix B). The resulting volume flux increases with Γ (Fig. 14).

In the models, Q_p appears implicitly in the expression of the buoyancy difference (19) as

$$Q_p = \alpha^{\frac{2}{3}} (1+\Gamma)^{-\frac{1}{3}} \left(z_I|_{x=-\frac{A}{2}} + \frac{1}{2} \right) = \begin{cases} \frac{1}{2} \alpha^{\frac{2}{3}} (1+\Gamma)^{-\frac{1}{3}}, & \text{for model 1,} \\ \frac{1}{2} \alpha^{\frac{2}{3}} (1+\Gamma)^{\frac{2}{3}}, & \text{for model 2.} \end{cases} \tag{22}$$

Notably, the models predict contrary trends for the volume flux with Γ. Model 1 is in conflict with the simulation data, showing a decrease of the volume flux with Γ, whereas model 2 correctly captures the observed trend of Q_p.

The decrease of the volume flux with growing Γ in model 1 is due to the decreasing velocity of the plumes [Fig. 8(b)], since the plume velocity obeys $w_m \propto (1+\Gamma)^{-\frac{1}{3}}$ (see Appendix A). In model 2, the decreasing plume velocity is countered by the growing height of the plume, $\frac{1}{2} + z_p \propto 1 + \Gamma$, and a correspondingly growing width of the plume at the interface level. The effect of the increasing area through which the plume discharges fluid to the adjoining layer on Q_p dominates over that of the decreasing plume velocity and leads to a volume flux increasing with Γ.

The volume flux of model 2 is in good agreement with the DNS data for buoyancy flux ratios $\Gamma \leqslant 0.23$, until the volume flux from the DNS data increases abruptly at $\Gamma = 0.39$. The abrupt increase of the volume flux coincides with the disappearance of the secondary circulation cells and the increased vertical stratification of the buoyancy field in the layers between $\Gamma = 0.23$ and 0.39 in comparison to $\Gamma < 0.23$ (Figs. 7 and 6). The vertical stratification is not realized in the models and might account for the deviation of the second model's volume flux from the DNS data.

Combining (19) and (22), the buoyancy difference of model 1 and 2 is

$$\Delta b(Q_p) = (1-\Gamma)(1+\Gamma)^{-1} Q_p^{-1}. \tag{23}$$

Inserting the volume flux from the DNS data into the models (23), we find that the corrected volume flux has little impact on the value of Δb (Fig. 12), since Q_p stands in the denominator in Eq. (23) and the abrupt increase in Q_p is small relative to the overall magnitude of Q_p.

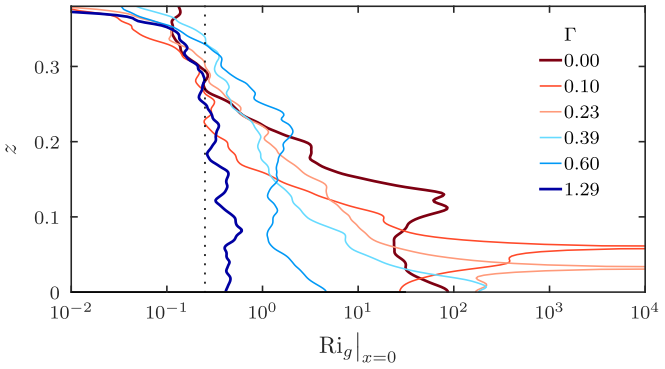

FIG. 15. Gradient Richardson number Ri_g along a vertical slice in the middle of the domain ($x = 0$). The value $\mathrm{Ri}_g = \frac{1}{4}$ is marked by a dotted line. At the chosen position $x = 0$, the interface elevation is $z = 0$ for all configurations.

D. The gradient Richardson number at the interface

To investigate the impact of the shear flow on the interface between the layers, we define a gradient Richardson number:

$$\mathrm{Ri}_g(x, z) \equiv \frac{\partial_z \overline{b}}{(\partial_z \overline{u})^2}. \tag{24}$$

In inviscid nonturbulent parallel flows, a stratified shear profile is linearly stable if the gradient Richardson number exceeds the critical value of $\frac{1}{4}$ everywhere [22,23]. Gradient Richardson numbers with values approximately independent of time and the flow-normal direction [24–30] have been interpreted as an indicator of a turbulent equilibrium state [28]. In this context, it has been proposed that turbulent shear flows are attracted to a state of marginal instability, which is marked by a gradient Richardson number $\mathrm{Ri}_g \approx \frac{1}{4}$ [27,31].

In the present paper, the profiles of the gradient Richardson number $\mathrm{Ri}_g(0, z)$ in the horizontal middle of the domain far exceed those expected for marginal stability ($\frac{1}{4}$) at the interface ($z = 0$) and in its vicinity for all simulations for which $\Gamma \leqslant 0.39$ (Fig. 15). Thus, the stabilizing effect of the stratification is (significantly) larger than the destabilizing effect of the shear flow. The reason is that the background stratification for the shear flow is not created by local mixing, but externally by the plumes on the side walls and the convection from the distributed buoyancy flux sources, which jointly determine both the horizontal velocity and the buoyancy difference. Equivalently, the turbulence that disturbs the buoyancy interface [Figs. 4(a)–4(e)] does not originate from the interface but arises from the plumes and the convection from distributed sources.

The gradient Richardson number $\mathrm{Ri}_g(0, 0)$ at the interface changes with the buoyancy flux ratio Γ (Fig. 15). For $\Gamma \leqslant 0.23$, there exists no monotonic relationship between $\mathrm{Ri}_g(0, 0)$ and Γ; however, $\mathrm{Ri}_g(0, 0)$ decreases with Γ for large $\Gamma \geqslant 0.39$. The nonmonotonic behavior of $\mathrm{Ri}_g(0, 0)$ for $\Gamma \leqslant 0.23$ originates from the mean horizontal velocity $\overline{u}(0, z)$, the profile of which varies close to the interface due to the changing width of the secondary circulation cells with Γ (see Sec. IV B). The peaks in $\mathrm{Ri}_g(0, z)$ for $\Gamma = 0.10$ and 0.23 correspond to a sign change in $\partial_z \overline{u}(0, z)$ close to the interface [local minima in Fig. 8(a)], which appears as the secondary circulation cells intersect the plane $x = 0$.

We can establish a relationship between Γ and the gradient Richardson number at the interface by denoting the width of the shear layer as ℓ_U and the width of the buoyancy interface as ℓ_b and

estimating (24) at the interface as

$$\mathrm{Ri}_g|_{z=z_\mathrm{I}} \approx \frac{\Delta b}{\Delta U^2}\,\frac{\ell_U^2}{\ell_b} = \frac{1}{16}\,\frac{\Delta b}{Q_\mathrm{p}^2}\,\frac{\ell_U^2}{\ell_b}. \tag{25}$$

Here, Δb and ΔU are the characteristic differences in buoyancy and horizontal velocity between the layers, respectively. The second identity in Eq. (25) results from estimating the absolute value of the horizontal velocity in the layers as $U = 2\,Q_\mathrm{p}$, using the plume volume flux Q_p and the layer depth $\frac{1}{2}$ at $x = 0$, and taking $\Delta U = 2\,U$. Utilizing model 2 for Δb (19) and Q_p (22) we obtain

$$\mathrm{Ri}_g|_{z=z_\mathrm{I}} \approx \frac{1}{2}\,\alpha^{-2}\,(1-\Gamma)\,(1+\Gamma)^{-3}\,\frac{\ell_U^2}{\ell_b}. \tag{26}$$

The layer depths ℓ_b and ℓ_U cannot be determined by the models. However, we expect them to depend on the turbulence from the plumes and the convective instabilities from the distributed sources of buoyancy flux. As such, ℓ_b and ℓ_U would be functions of Γ, rather than emerging naturally without a dependence on Γ from a state of marginal stability.

VII. CONCLUSIONS

Localized sources of buoyancy at the top and bottom boundary of a closed domain produce turbulent plumes that maintain a stable two-layer stratification in the steady state. The addition of distributed heating leads to a competition between the stabilizing effect of the localized sources and the destabilizing effect of the distributed sources. The ratio of the distributed to the localized buoyancy flux, Γ, determines the system's response. At $\Gamma < 1$, the stabilizing effect of the localized sources dominates and the buoyancy field is stably stratified in two layers. The buoyancy difference between the layers decreases with increasing Γ, until the two-layer stratification is destroyed for $\Gamma > 1$. These remarks are consistent with the results of Wells, Griffiths, and Turner [10] for different configurations of combined localized and distributed heating in a closed domain [Figs. 1(a) and 1(b)]. The buoyancy transport between the layers of the two-layer stratification ($\Gamma < 1$) is dominated by the plumes. This agrees with the negligible interfacial buoyancy flux inferred by Partridge and Linden [13] for a naturally ventilated domain heated by a localized and a distributed source [Fig. 1(d)], which contrasts with Chenvidyakarn and Woods [11] [Fig. 1(c)].

Despite its focus on stably stratified states dominated by localized sources ($\Gamma < 1$), our paper demonstrates the significance of distributed heating in determining the flow circulation and buoyancy structure. Distributed heating produces a lateral buoyancy gradient in each layer, which increases with Γ. A result of the lateral buoyancy gradient is a tilting of the interface separating the two layers, which increases with Γ. The tilt of the interface affects the secondary circulations that develop within each layer and the strength of the primary large-scale circulation.

In predictions of the buoyancy difference Δb between the layers, the lateral buoyancy gradient can be neglected for small values of Γ, but plays an essential role when $\Gamma \gtrapprox 0.23$. In contrast, the lateral buoyancy gradient is crucial in predictions of the strength of the large-scale circulation for all values of $\Gamma < 1$. Indeed, our model predicts that the height at which the plumes penetrate the interface, which determines their volume flux, is solely a function of Γ. In this regard we note that the two-layer stratification disappears as the plume height becomes comparable to the domain height.

The configuration considered in this paper is relatively simple and might therefore provide a useful starting point in the investigation of nonuniformly heated domains. In all such cases we would expect to find a buoyancy structure that is more stably stratified than the well-mixed environments produced by uniform heating. In the case of combinations of localized and distributed sources that are not the same on the bottom and top of the domain, we would not necessarily expect to find the resulting interface at the domain's midplane. Conservation of volume suggests that in such cases the interface would position itself to balance the interfacial volume flux from each plume.

Predicting the effects of different heating distributions finds application in inverse problems relating to the estimation of boundary heat fluxes from temperature measurements. Such estimates are of particular interest in building design and heating control, where the parameters that determine heat transfer might be difficult to determine [32]. The models presented in this paper could be utilized in such a context to infer boundary heating from a limited number of temperature measurements.

ACKNOWLEDGMENTS

This work was supported by the Skempton Award from the Department of Civil and Environmental Engineering, Imperial College London. Computational resources for this work have been provided by the "Cambridge Service for Data Driven Discover" system operated by the University of Cambridge Research Computing Service funded by Engineering and Physical Sciences Research Council Tier-2 Capital Grant No. EPP0202591 and by the High Performance Computing facility at Imperial College London.

APPENDIX A: PLANAR PLUMES

We consider wall-bounded planar plumes in an unstratified quiescent environment from a source of buoyancy flux F_ℓ. At an elevation ζ sufficiently far above the plume source to consider the source as one-dimensional, the plume's buoyancy flux $\widetilde{F}$ relative to the ambient of the plume, the volume flux Q, and momentum flux M can be modeled as

$$\widetilde{F} = F_\ell, \quad Q(\zeta) = \alpha^{\frac{2}{3}} F_\ell^{\frac{1}{3}} \zeta, \quad M(\zeta) = \alpha^{\frac{1}{3}} F_\ell^{\frac{2}{3}} \zeta, \tag{A1}$$

with

$$\widetilde{F}(\zeta) = \int_{\mathcal{I}} \overline{w\,\widetilde{b}}(x,\zeta)\,dx, \quad Q(\zeta) = \int_{\mathcal{I}} \overline{w}(x,\zeta)\,dx, \quad M(\zeta) = \int_{\mathcal{I}} \overline{w^2}(x,\zeta)\,dx. \tag{A2}$$

Here, α is the entrainment coefficient such that $\frac{dQ}{d\zeta} = \alpha \frac{M}{Q}$; $\widetilde{b} \equiv b - b_\mathrm{a}$ is the relative buoyancy of the plume to its ambient of buoyancy b_a. The domain $\mathcal{I}$ is the interval that corresponds to the horizontal extent of the plume. The model (A1) is equivalent to the model of a wall-bounded axisymmetric plume by Ezhova, Cenedese, and Brandt [33], where we neglect wall-shear stress due to the free-slip condition imposed on the side walls of our simulated domain. The resulting expressions for $\widetilde{F}$, Q, and M (A1) correspond to those describing an unconfined plume of half the source strength F_ℓ and half the width (see, e.g., [20]). The effect of the side walls and confinement on the plumes will be addressed at the end of this section.

In the following, we consider the vertical flow arising from purely localized heating ($\Gamma = 0$) with respect to plume scaling relations. All simulation data correspond to the left-hand plume. We define the integral quantities in Eq. (A2) by taking the integration interval $\mathcal{I}$ to be one half of the domain, $\mathcal{I}_1 = [-\frac{\Lambda}{2}, 0]$ (blue curves in Fig. 16). This approach relies on the assumption that the vertical velocity outside the plume is negligible. The resulting volume flux [blue curve in Fig. 16(a)] indicates that this assumption is not suitable. Close to $x = 0$, the secondary circulations induce a non-negligible vertical velocity component in the mean flow of both layers [Fig. 7(a)], which leads to a volume flux profile in the lower layer ($z < 0$) that is not consistent with plume scaling (A1).

A more suitable integration interval is $\mathcal{I}_2 = [-\frac{\Lambda}{2}, x_\psi]$, where the point (x_ψ, z_ψ) marks the center of the left-hand secondary circulation, manifest as a local extremum of the stream function. The interval $\mathcal{I}_2$ can be understood as the smallest integration interval of constant width which contains the plume and the adjoining jet. Using $\mathcal{I}_2$, we obtain a volume flux which scales according to (A1) up to $z \approx 0$, where the plume penetrates the interface between the layers [Fig. 16(a), red curve].

In Fig. 16(b), the displayed buoyancy flux is calculated as

$$\widetilde{F} = \int_{\mathcal{I}} \overline{w}\,(\overline{b} - \overline{b}_\mathrm{a}) + \overline{w'\,b'}\,dx, \tag{A3}$$

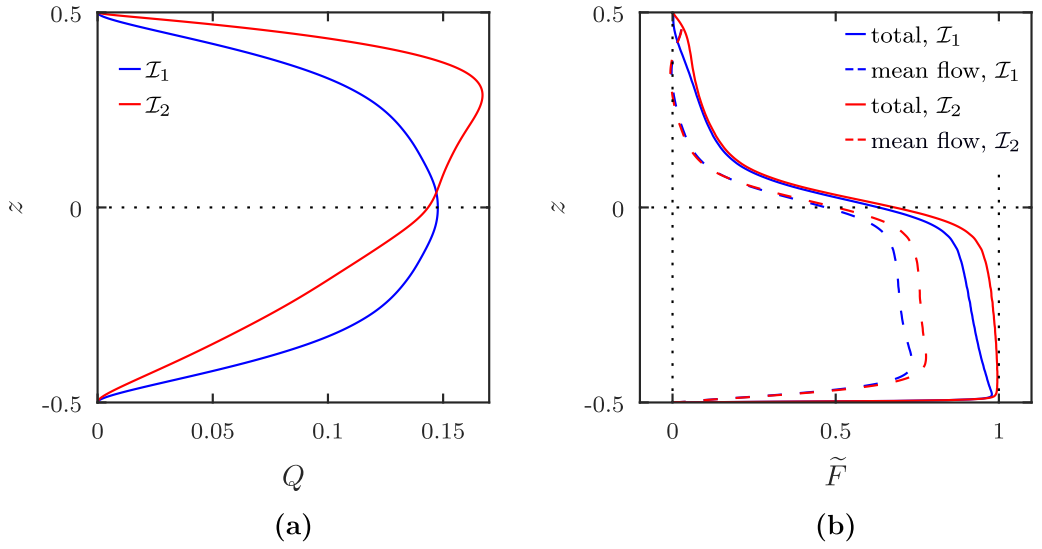

FIG. 16. Scaling of the plume's (a) volume flux Q and (b) relative buoyancy flux $\widetilde{F}$ at $\Gamma = 0$. Both the total buoyancy flux $\widetilde{F}$ of the plume and its contribution from the mean flow are shown. $\widetilde{F}$ and Q are calculated from (A2) and (A3), respectively, for two integration intervals, $\mathcal{I}_1$ and $\mathcal{I}_2$ (see text).

with the ambient buoyancies $\overline{b}_{\mathrm{a}1}$ and $\overline{b}_{\mathrm{a}2}$ for the intervals $\mathcal{I}_1$ and $\mathcal{I}_2$, respectively, being defined as

$$\overline{b}_{\mathrm{a}1} \equiv 2\,\Lambda^{-1} \int_{\mathcal{I}_1} \overline{b}\,dx, \quad \overline{b}_{\mathrm{a}2} \equiv |x_\psi|^{-1}\Big[\int_{\mathcal{I}_1} \overline{b}\,dx - \int_{\mathcal{I}_2} \overline{b}\,dx\Big]. \tag{A4}$$

The relative buoyancy flux differs only slightly between the two integration intervals [Fig. 16(b)]. In agreement with (A1), the relative buoyancy flux in the lower layer is approximately constant at the buoyancy flux value $F_\ell = 1$ of the localized source. At the bottom boundary $\widetilde{F}(-\frac{1}{2}) = 0 \neq F_\ell$, since $\widetilde{F}$ does not include a diffusive buoyancy flux. As the plume penetrates the interface between the layers ($z \approx 0$), $\widetilde{F}$ decreases abruptly, but does not reduce to zero. In contrast, the mean flow contribution to $\widetilde{F}$ goes to zero in the upper layer ($z > 0$). Thus, the flow in the upper layer corresponds to a jet in the sense of integrals of mean quantities $\overline{b}$ and $\overline{w}$ [8], but carries a residual buoyancy flux as a result of $\overline{w'b'}$.

To evaluate the models of Sec. V, we require the value of the plume entrainment coefficient. Two independent estimates of the entrainment coefficient can be deduced from observations, using the plume equations (A1) [8]. Inverting the expression for the volume flux in Eq. (A1) at the interface $z = 0$, i.e., $\zeta = \frac{1}{2}$, we define an entrainment coefficient:

$$\alpha_Q \;\equiv\; {F_\ell}^{-\frac{1}{2}} \left(\frac{1}{2}\right)^{-\frac{3}{2}} Q\big(\tfrac{1}{2}\big)^{\frac{3}{2}} \;=\; 2^{\frac{3}{2}}\, {F_\ell}^{-\frac{1}{2}} \left(\int_{-\frac{\Lambda}{2}}^{0} \overline{w}\big(x,\tfrac{1}{2}\big)\,dx\right)^{\frac{3}{2}}. \tag{A5}$$

We use $\mathcal{I}_1$ for simplicity, as the difference to the result from $\mathcal{I}_2$ is small at $z = 0$ [Fig. 16(a)].

Assuming plumes of width r_m with top-hat profiles of velocity w_m and relative buoyancy $\widetilde{b}_m$, we obtain from (A1)

$$r_m(\zeta) = \alpha\,\zeta, \quad w_m(\zeta) = \alpha^{-\frac{1}{3}} {F_\ell}^{\frac{1}{3}} \;=\; \text{const}, \quad \widetilde{b}_m(\zeta) = \alpha^{-\frac{2}{3}}\, {F_\ell}^{\frac{2}{3}}\, \zeta^{-1}, \tag{A6}$$

where we neglect turbulent contributions to the relative buoyancy flux. Inverting the expression for $\widetilde{b}_m$ at $\zeta = \frac{1}{2}$, we define a second approximation of the entrainment coefficient:

$$\alpha_b \;\equiv\; F_\ell \left(\frac{1}{2}\right)^{-\frac{3}{2}} \widetilde{b}_m\big(\tfrac{1}{2}\big)^{-\frac{3}{2}} \;=\; F_\ell \left(\frac{1}{2}\right)^{-\frac{3}{2}} \Delta b^{-\frac{3}{2}}. \tag{A7}$$

TABLE I. Literature values for the entrainment coefficient of planar plumes from experiments. Given are the values of the entrainment coefficient α' as defined in the respective publication and of the corresponding α consistent with the definition used in the present paper, i.e., $\frac{dQ}{d\zeta} = 2\,\alpha\,\frac{M}{Q}$ for free plumes and $\frac{dQ}{d\zeta} = \alpha\,\frac{M}{Q}$ for wall-bounded plumes.

			α'	α
Free plumes	Lee and Emmons [34]	$\alpha = \sqrt{2}\,\alpha'$	0.16	0.23
	Kotsovinos [35]	$\alpha = \sqrt{2}\,\alpha'$	0.11	0.16
	Ramaprian and Chandrasekhara [36]	$\alpha = \alpha'/\sqrt{2}$	0.23	0.16
	Yuana and Cox [37]	$\alpha = \sqrt{2}\,\alpha'$	0.13	0.18
	Parker *et al.* [38]	$\alpha = \alpha'$	0.14	0.14
Wall-bounded plumes	Grella and Faeth [39]	$\alpha = \sqrt{2}\,\alpha'$	0.067	0.095
	Lai and Faeth [40]	$\alpha = \sqrt{2}\,\alpha'$	0.071	0.100
	Sangras *et al.* [41]	$\alpha = \sqrt{2}\,\alpha'$	0.068	0.096
	Parker *et al.* [38]	$\alpha = \alpha'$	0.08	0.08

The buoyancy of a layer corresponds to the buoyancy of its supplying plume where it penetrates the interface. Therefore, the relative buoyancy of the plume at the interface is $\widetilde{b}_m(\frac{1}{2}) = \overline{b}_\mathrm{a} - (-\overline{b}_\mathrm{a}) = \Delta b$, where Δb is the distance between the peaks of the buoyancy field's PDF.

The entrainment coefficients can be estimated from the DNS data via (A5) and (A7) as

$$\alpha_Q \approx 0.161, \quad \alpha_b \approx 0.169. \tag{A8}$$

The good agreement between the two entrainment coefficients α_Q and α_b confirms that the vertical flows from the line sources at $\Gamma = 0$ can be modeled as planar plumes from sources at $z = \pm\frac{1}{2}$. The agreement between both values also attests to a sufficiently small width λ of the localized sources for them to act as virtual line sources. The buoyancy based entrainment coefficient α_b is slightly larger than α_Q, possibly due to the neglected term of turbulent buoyancy transport in Eq. (A6). Accordingly, the value of α_Q is used as the entrainment coefficient in this paper.

While the macroscopic characteristics of a wall-bounded plume can be modeled similarly to those of a plume in an unconstrained environment (A1), a turbulent flow along a wall differs from a freely evolving one. The entrainment of wall-bounded plumes is significantly reduced compared to free plumes, with an entrainment coefficient slightly larger than half of that of a free plume [38]. The adjoining wall prevents the large-scale wavering motion present in free plumes [38], thus reducing mixing, and has been proposed to suppress cross-stream turbulent fluxes [41].

The entrainment coefficient $\alpha \approx 0.161$ we obtain is closer in magnitude to values of α typical for free planar plumes than to those of wall-bounded plumes (Table I). This might partly be due to the wall-shear stress, which is nonzero in all experimental realizations of wall-bounded plumes (Table I), but disappears in our configurations because of free-slip boundaries. Parker *et al.* [38] expect an increased entrainment with reduced wall-shear stress. A second factor that potentially increases plume entrainment is our specific configuration of two confined plumes connected by a large-scale circulation with background turbulence. In a related setup of confined axisymmetric plumes, Craske and Davies Wykes [8] observed entrainment coefficients of slightly less than twice the value typical for unconfined axisymmetric plumes, noting that background turbulence disrupts the near-source necking of lazy plumes.

APPENDIX B: INTERFACE BETWEEN THE LAYERS OF THE STABLE STRATIFICATION

The two layers of the stable stratification ($\Gamma < 1$) are separated by an interface at zero buoyancy. This isosurface is generally tilted and shows a local maximum or minimum in z close to where the plumes penetrate the interface. Figure 17 shows an example of the buoyancy field, with the isosurface's extrema marked as points B and C. We define the interface between the two layers as

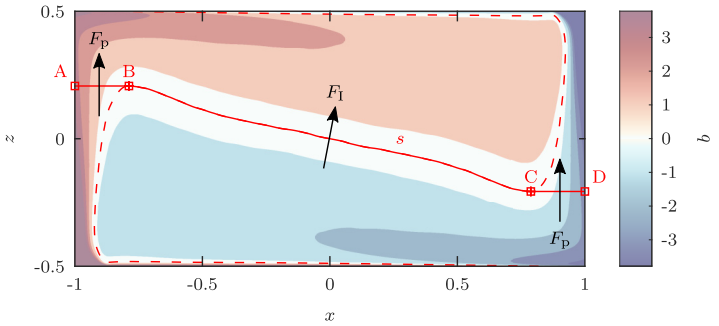

FIG. 17. Schematic for the definition of a separating surface between the two layers of the stratification, using the mean buoyancy field. The red dashed line marks the isosurface at zero buoyancy. The solid red line corresponds to the separating curve s (see text).

the isosurface of zero buoyancy between its local extrema, i.e., $\overline{\mathrm{BC}}$. We continue the curve of the interface from B and C by horizontal segments to the left and right, respectively, which intersect the vertical boundaries at points A and D. Buoyancy exchanged between the two layers of the stratification is either transported across the interface, $\overline{\mathrm{BC}}$, or via the the plumes, i.e., across $\overline{\mathrm{AB}}$ and $\overline{\mathrm{CD}}$. The entire curve over the points A, B, C, and D will be denoted as s.

The buoyancy flux across an arbitrary surface S can be calculated as

$$F_S = \frac{1}{\Lambda_y} \int_S \sum_i f_i \, n_i \, dS, \tag{B1}$$

where $f_i = u_i \, b - \mathrm{Pe}^{-1} \, \partial_i b$ is the local buoyancy flux in the spatial direction specified by i and n_i are the components of the unit vector perpendicular to the surface. Thus, the mean buoyancy flux between the two layers, calculated across the separating curve s, is

$$F_s = \int_{-\frac{\Lambda}{2}}^{\frac{\Lambda}{2}} \left[-\frac{dz_s}{dx} \cdot \overline{f}_x(x, z_s(x)) + \overline{f}_z(x, z_s(x)) \right] dx \equiv \int_{-\frac{\Lambda}{2}}^{\frac{\Lambda}{2}} f_s(x) \, dx, \tag{B2}$$

with f_s defined as the corresponding mean local buoyancy flux. Here, $z_s(x)$ is the elevation of the separating curve s. The buoyancy flux F_s is well defined, since z_s is differentiable at the junction of the segments $\overline{\mathrm{AB}}$, $\overline{\mathrm{BC}}$, and $\overline{\mathrm{CD}}$.

Separating the buoyancy flux F_s into the buoyancy transport of the two plumes and the buoyancy transport across the interface, $F_s = 2\,F_\mathrm{p} + F_\mathrm{I}$, we define

$$F_\mathrm{p} = \frac{1}{2} \int_{-\frac{\Lambda}{2}}^{x_\mathrm{A}} f_s(x) \, dx + \frac{1}{2} \int_{x_\mathrm{B}}^{\frac{\Lambda}{2}} f_s(x) \, dx, \quad F_\mathrm{I} = F_s - 2\,F_\mathrm{p}. \tag{B3}$$

Equivalently, the volume flux of the plumes is determined from the simulation data as

$$Q_\mathrm{p} = \frac{1}{2} \int_{-\frac{\Lambda}{2}}^{x_\mathrm{A}} \overline{w}(x) \, dx + \frac{1}{2} \int_{x_\mathrm{B}}^{\frac{\Lambda}{2}} \overline{w}(x) \, dx. \tag{B4}$$

[1] P. F. Linden, G. F. Lane-Serff, and D. A. Smeed, Emptying filling boxes: The fluid mechanics of natural ventilation, J. Fluid Mech. **212**, 309 (1990).

[2] G. G. Rooney and P. F. Linden, Strongly buoyant plume similarity and "small-fire" ventilation, Fire Safety J. **29**, 235 (1997).

[3] P. F. Linden and P. Cooper, Multiple sources of buoyancy in a naturally ventilated enclosure, J. Fluid Mech. **311**, 177 (1996).
[4] P. F. Linden and N. B. Kaye, Interacting turbulent plumes in a naturally ventilated enclosure, Int. J. Ventilation **4**, 301 (2006).
[5] B. R. Morton, G. Taylor, and J. S. Turner, Turbulent gravitational convection from maintained and instantaneous sources, Proc. R. Soc. A **234**, 1 (1956).
[6] W. D. Baines and J. S. Turner, Turbulent buoyant convection from a source in a confined region, J. Fluid Mech. **37**, 51 (1969).
[7] M. G. Worster and H. E. Huppert, Time-dependent density profiles in a filling box, J. Fluid Mech. **132**, 457 (1983).
[8] J. Craske and M. S. Davies Wykes, The entrainment and energetics of turbulent plumes in a confined space, J. Fluid Mech. **883**, A2 (2020).
[9] G. Ahlers, S. Grossmann, and D. Lohse, Heat transfer and large scale dynamics in turbulent Rayleigh-Bénard convection, Rev. Mod. Phys. **81**, 503 (2009).
[10] M. G. Wells, R. W. Griffiths, and J. S. Turner, Competition between distributed and localized buoyancy fluxes in a confined volume, J. Fluid Mech. **391**, 319 (1999).
[11] T. Chenvidyakarn and A. W. Woods, On underfloor air-conditioning of a room containing a distributed heat source and a localised heat source, Energy and Buildings **40**, 1220 (2008).
[12] G. R. Hunt, J. M. Holford, and P. F. Linden, Natural ventilation by the competing effects of localised and distributed heat sources, *Proceedings of the 14th Australasian Fluid Mechanics Conference* (Causal Productions Pty Ltd, Australia, 2001).
[13] J. L. Partridge and P. F. Linden, Steady flows in a naturally-ventilated enclosure containing both a distributed and a localised source of buoyancy, Building Environment **125**, 308 (2017).
[14] J. Craske and M. van Reeuwijk, Energy dispersion in turbulent jets. Part 1. Direct simulation of steady and unsteady jets, J. Fluid Mech. **763**, 500 (2015).
[15] R. Verstappen and A. Veldman, Symmetry-preserving discretization of turbulent flow, J. Comput. Phys. **187**, 343 (2003).
[16] M. V. Pham, F. Plourde, and S. D. Kim, Effect of swirl on pure turbulent thermal plume development, Int. J. Heat Fluid Flow **27**, 502 (2006).
[17] M. van Reeuwijk, H. J. J. Jonker, and K. Hanjalić, Identification of the wind in Rayleigh-Bénard convection, Phys. Fluids **17**, 051704 (2005).
[18] C. Sun, K.-Q. Xia, and P. Tong, Three-dimensional flow structures and dynamics of turbulent thermal convection in a cylindrical cell, Phys. Rev. E **72**, 026302 (2005).
[19] N. E. Kotsovinos and E. J. List, Plane turbulent buoyant jets. Part 1. Integral properties, J. Fluid Mech. **81**, 25 (1977).
[20] T. S. van den Bremer and G. R. Hunt, Two-dimensional planar plumes and fountains, J. Fluid Mech. **750**, 210 (2014).
[21] C. B. Vreugdenhil, *Numerical Methods for Shallow-Water Flow* (Springer, New York, 1994).
[22] J. W. Miles, On the stability of heterogeneous shear flows, J. Fluid Mech. **10**, 496 (1961).
[23] L. N. Howard, Note on a paper of John W. Miles, J. Fluid Mech. **10**, 509 (1961).
[24] J. J. Rohr, E. C. Itsweire, K. N. Helland, and C. W. V. Atta, Growth and decay of turbulence in a stably stratified shear flow, J. Fluid Mech. **195**, 77 (1988).
[25] S. E. Holt, J. R. Koseff, and J. H. Ferziger, A numerical study of the evolution and structure of homogeneous stably stratified sheared turbulence, J. Fluid Mech. **237**, 499 (1992).
[26] L. H. Shih, J. R. Koseff, J. H. Ferzinger, and C. R. Rehmann, Scaling and parameterization of stratified homogeneous turbulent shear flow, J. Fluid Mech. **412**, 1 (2000).
[27] W. D. Smyth and J. N. Moum, Marginal instability and deep cycle turbulence in the eastern equatorial pacific ocean, Geophys. Res. Lett. **40**, 6181 (2013).
[28] Q. Zhou, J. R. Taylor, and C. P. Caulfield, Self-similar mixing in stratified plane Couette flow for varying Prandtl number, J. Fluid Mech. **820**, 86 (2017).
[29] H. Salehipour, W. R. Peltier, and C. P. Caulfield, Self-organized criticality of turbulence in strongly stratified mixing layers, J. Fluid Mech. **856**, 228 (2018).

[30] M. van Reeuwijk, M. Holzner, and C. P. Caulfield, Mixing and entrainment are suppressed in inclined gravity currents, J. Fluid Mech. **873**, 786 (2019).
[31] S. A. Thorpe and Z. Liu, Marginal instability? J. Phys. Oceanogr. **39**, 2373 (2009).
[32] J. Brouns, A. Nassiopoulos, F. Bourquin, and K. Limam, Dynamic building performance assessment using calibrated simulation, Energy and Buildings **122**, 160 (2016).
[33] E. Ezhova, C. Cenedese, and L. Brandt, Dynamics of three-dimensional turbulent wall plumes and implications for estimates of submarine glacier melting, J. Phys. Oceanogr. **48**, 1941 (2018).
[34] S.-L. Lee and H. W. Emmons, A study of natural convection above a line fire, J. Fluid Mech. **11**, 353 (1961).
[35] N. E. Kotsovinos, A study of the entrainment and turbulence in a plane buoyant jet, Tech. Report, California Institute of Technology, 1975).
[36] B. R. Ramaprian and M. S. Chandrasekhara, Measurements in vertical plane turbulent plumes, J. Fluids Eng. **111**, 69 (1989).
[37] L.-M. Yuana and G. Cox, An experimental study of some line fires, Fire Safety J. **27**, 123 (1996).
[38] D. A. Parker, H. C. Burridge, J. L. Partridge, and P. F. Linden, A comparison of entrainment in turbulent line plumes adjacent to and distant from a vertical wall, J. Fluid Mech. **882**, A4 (2020).
[39] J. J. Grella and G. M. Faeth, Measurements in a two-dimensional thermal plume along a vertical adiabatic wall, J. Fluid Mech. **71**, 701 (1975).
[40] M.-C. Lai and G. M. Faeth, Turbulence structure of vertical adiabatic wall plumes, J. Heat Transfer **109**, 663 (1987).
[41] R. Sangras, Z. Dai, and G. M. Faeth, Velocity statistics of plane self-preserving buoyant turbulent adiabatic wall plumes, J. Heat Transfer **122**, 693 (2000).